Available online at www.sciencedirect.com
ScienceDirect
Journal of Solid State Chemistry 180 (2007) 2420–2428
JOURNAL OF SOLID STATE CHEMISTRY
www.elsevier.com/locate/jssc

Structural and physical properties of $Mg_{3-x}Zn_xSb_2$ ($x = 0$–1.34)

Faraz Ahmadpour[a], Taras Kolodiazhnyi[b], Yurij Mozharivskyj[a,*]

[a]*Department of Chemistry, McMaster University, 1280 Main Street West, Hamilton, Ontario, Canada L8S 4M1*
[b]*National Institute for Materials Science, 1-1 Namiki, Tsukuba, Ibaraki 305-0044, Japan*

Received 27 April 2007; received in revised form 13 June 2007; accepted 16 June 2007
Available online 23 June 2007

Abstract

The $Mg_{3-x}Zn_xSb_2$ phases with $x = 0$–1.34 were prepared by direct reactions of the elements in tantalum tubes. According to the X-ray single crystal and powder diffraction, the $Mg_{3-x}Zn_xSb_2$ phases crystallize in the same $P\bar{3}m1$ space group as the parent Mg_3Sb_2 phase. The $Mg_{3-x}Zn_xSb_2$ structure is different from the other substituted structures of Mg_3Sb_2, such as (Ca, Sr, Ba) Mg_2Sb_2 or $Mg_{5.23}Sm_{0.77}Sb_4$, in a way that in $Mg_{3-x}Zn_xSb_2$ the Mg atoms on the tetrahedral sites are replaced, while in the other structures Mg on the octahedral sites is replaced. Thermoelectric performance for the two members of the series, Mg_3Sb_2 and $Mg_{2.36}Zn_{0.64}Sb_2$, was evaluated from low to room temperatures through resistivity, Seebeck coefficient and thermal conductivity measurements. In contrast to Mg_3Sb_2 which is a semiconductor, $Mg_{2.36}Zn_{0.64}Sb_2$ is metallic and exhibits an 18-times larger dimensionless figure-of-merit, ZT, at room temperature. However, thermoelectric performance of $Mg_{2.36}Zn_{0.64}Sb_2$ is still poor and it is mostly due to its large electrical resistivity.

Keywords: Magnesium zinc antimonide; Structure; Electrical resistivity; Thermal conductivity; Thermoelectric properties

1. Introduction

Outstanding properties of the state-of-the-art thermoelectric material β-"Zn_4Sb_3" are attributed to its very low thermal conductivity (~0.9 W/K m at 293 K) [1] which approaches that of amorphous solids. At elevated temperatures, above 423 K, β-"Zn_4Sb_3" outperforms other state-of-the-art thermolectric materials, such as Bi_2Te_3 and $CeFe_4Sb_{12}$ [2]. Elucidation of the crystal structure of β-"Zn_4Sb_3" revealed that such low thermal conductivity stems from large atomic deficiencies (~10%) on the main Zn site and presence of additional, partially occupied Zn sites in β-"Zn_4Sb_3" [2,3]. Interesting feature of β-"Zn_4Sb_3" is that the Zn atoms seem to be relatively mobile in the structure. At low-temperatures, below the $\beta \rightarrow \alpha$ transition of ~259 K, single crystal studies indicated full ordering of the Zn atoms and yielded the stoichiometric $Zn_{13}Sb_{10}$ composition [4]. This $Zn_{13}Sb_{10}$ composition was later verified using microprobe analysis of the flux-grown crystals [5]. On the other hand, at high temperatures the Zn atoms "escape" from the structure. As shown by high-temperature powder diffraction experiments, the polycrystalline phase starts to loose Zn above 473 K in dynamic vacuum, resulting in ZnSb and subsequently in Sb upon further increases in temperature [6]. It was also shown that a single crystal of $Zn_{13}Sb_{10}$, sealed with argon inside a glass capillary, decomposed into ZnSb + Zn even upon relatively fast heating to 773 K [5].

Since such instability may pose challenges for applications of $Zn_{13}Sb_{10}$, we looked into ways of improving temperature stability of $Zn_{13}Sb_{10}$ through chemical substitution while maintaining its electronic structure. One of the possibilities explored by us was the Mg substitution. In combination with the *p*-elements, Mg usually accepts the 2+ oxidation state, e.g. MgS [7], and is also found to occupy tetrahedral sites, e.g. Mg_3Sb_2 [7], similarly to Zn in $Zn_{13}Sb_{10}$ [8]. However, experimental attempts on the Mg substitution, even partial, for $Zn_{13}Sb_{10}$ were not successful. Instead of the desired product we were getting mixtures of ZnSb and a Mg_3Sb_2-type phase. X-ray diffraction experiments performed on a crystal extracted from the $Zn_{10}Mg_3Sb_{10}$ sample yielded a structure similar to that of Mg_3Sb_2 and with the $Mg_{2.23(1)}Zn_{0.77(1)}Sb_2$ composition. In

*Corresponding author. Fax: +1 905 521 2773.
E-mail address: mozhar@mcmaster.ca (Y. Mozharivskyj).

0022-4596/$ - see front matter © 2007 Elsevier Inc. All rights reserved.
doi:10.1016/j.jssc.2007.06.011

this paper, we report on the structure and low-temperature physical properties of $Mg_{3-x}Zn_xSb_2$. Some studies were done on Mg_3Sb_2 but they focused on the high-temperature thermoelectric properties [9,10]. In course of the discussion, we will compare our results with the literature ones.

2. Experimental

2.1. Synthesis and X-ray powder diffraction

Samples $Mg_{3-x}Zn_xSb_2$ with $x = 0$, 0.4, 0.8, 1.2, 1.6, 2 were prepared from pieces of Mg (99.98 wt%, Alfa Aesar), Zn (99.99 wt%, CERAC), Sb (99.999 wt%, CERAC). The mixtures were sealed in cleaned Ta tubes under Ar atmosphere. The Ta tubes were then sealed in evacuated silica tubes. The samples were heated to 900 °C at the rate of 100 °C/h, kept at this temperature for 2 h and quenched in cold water. The products looked homogenous, and the color gradually changed from black for Mg_3Sb_2 to silver for $MgZn_2Sb_2$, indicating a possible decrease in the energy band gap and a change from semiconducting to metallic behavior.

The sample homogeneity and composition were checked through X-ray powder diffraction. Diffraction profiles in the 4–80° 2θ range were recorded on a Huber image plate Guinier camera with a Cu$K\alpha_1$ radiation. The full-profile Rietveld refinement was performed to refine the lattice constants and composition of the major phase and to verify existence of impurities. In accordance with the single crystal results and based on the symmetry of Mg_3Sb_2 [7], the major phase in each sample was assigned the $P\bar{3}m1$ space group. The Zn atoms were introduced on the 2*d* Mg2 site based on the single crystal results and to account for relatively low temperature factors.

In all samples except for the $Mg_{2.2}Zn_{0.8}Sb_2$ one, a secondary phase was detected (Table 1 and Fig. 1). The $Mg_{1.4}Zn_{1.6}Sb_2$ sample contained a small amount of a secondary phase, which could not be identified against known binary and ternary compounds of Mg, Zn, Sb and Ta. Based on the visual analysis, the amount of this secondary phase can be estimated to be around few atomic percent. The $MgZn_2Sb_2$ sample contained the same secondary phase but in a much larger quantity. Also, the refined composition of the major Mg_3Sb_2-type phase from the $MgZn_2Sb_2$ sample was identical to that from the $Mg_{1.4}Zn_{1.6}Sb_2$ sample, thus indicating that the homogeneity range for the Mg_3Sb_2-type phases is unlikely to extend beyond the $Mg_{1.66(2)}Zn_{1.34(2)}Sb_2$ composition. The refined compositions and crystallographic parameters of the Mg_3Sb_2-type phase for all samples (except for the $MgZn_2Sb_2$ sample) are summarized in Tables 1–3 and in the Supporting information section.

The compositions of the prepared $Mg_{3-x}Zn_xSb_2$ phases was Mg richer than the loaded compositions, indicating that some zinc and antimony may either have reacted with the Ta tubes or have remained in elemental form. In case of the Mg_3Sb_2 sample, we have detected Ta_3Sb in the product; while in $Mg_{2.6}Zn_{0.4}Sb_2$, elemental Zn have been detected and "missing" antimony may have reacted with walls of the Ta tubing. As for $Mg_{1.8}Zn_{1.2}Sb_2$, we observed elemental Sb in the product, but we could not account for the smaller Zn concentration.

2.2. X-ray single crystal diffraction

Originally, the structure of the Zn-containing phases was solved on the crystal extracted from the $Zn_{10}Mg_3Sb_{10}$ sample. The structure was successfully refined in the $P\bar{3}m1$ space group with the $Mg_{2.23(1)}Zn_{0.77(1)}Sb_2$ composition (Table 4). The structural model obtained was used for the refinement of the $Mg_{1.94(4)}Zn_{1.06(4)}Sb_2$ crystal extracted from the $Mg_{1.8}Zn_{1.2}Sb_2$ sample. In both cases, the room-temperature X-ray diffraction data were collected on a Bruker SMART Apex CCD diffractometer with Mo$K\alpha$ radiation and processed using the Bruker software package [11]. Crystallographic data and atomic parameters are summarized in Tables 4 and 5. Further details of the crystal structure investigations can be obtained from the Fachinformationszentrum Karlsruhe, 76344 Eggenstein-Leopoldshafen, Germany (fax: +49-7247-808-666; e-mail: crysdata@fiz.karlsruhe.de) on quoting the depository CSD no. 417991 for $Mg_{2.23(1)}Zn_{0.77(1)}Sb_2$ and 417992 for $Mg_{1.94(4)}Zn_{1.06(4)}Sb_2$ and also from the Supporting information.

2.3. Thermal analysis

TG and DSC analysis (Fig. 2) were performed for the Mg_3Sb_2 and $Mg_{2.2}Zn_{0.8}Sb_2$ samples on a LINSEIS L81-I instrument. The samples were heated in alumina crucibles to 1413 and 1173 K, respectively, at 20 K/min in the stream of $Ar + H_2$ with the volume ratio of 15:1. Hydrogen was added to consume traces of oxygen in the chamber and, thus, to prevent samples oxidation. Mg_3Sb_2 starts to loose mass above 1273 K and $Mg_{2.2}Zn_{0.8}Sb_2$ above 923 K as indicated by mass drops in the TG curves and broad endothermic peaks in the DSC curves. Mg_3Sb_2 undergoes two phase transformations, one at 1109 K and another at 1192 K, and $Mg_{2.2}Zn_{0.8}Sb_2$ one phase transition at 815 K.

2.4. Hot pressing and EDS analysis of the hot-pressed samples

The samples obtained in the Ta tubes were not suitable for physical properties measurements because of their powder-like form. Powders of Mg_3Sb_2 and $Mg_{2.2}Zn_{0.8}Sb_2$ were ground and then hot pressed in 12 mm graphite die under argon for 2 h. Short pressing time and argon atmosphere were chosen to minimize possible elements sublimation. The annealing temperatures of 1073 K for Mg_3Sb_2 and 723 K for $Mg_{2.2}Zn_{0.8}Sb_2$ were deliberately chosen below the onset temperatures of the phase transformations detected during the thermal analyses. The hot-pressed pellet of Mg_3Sb_2 was very solid and could

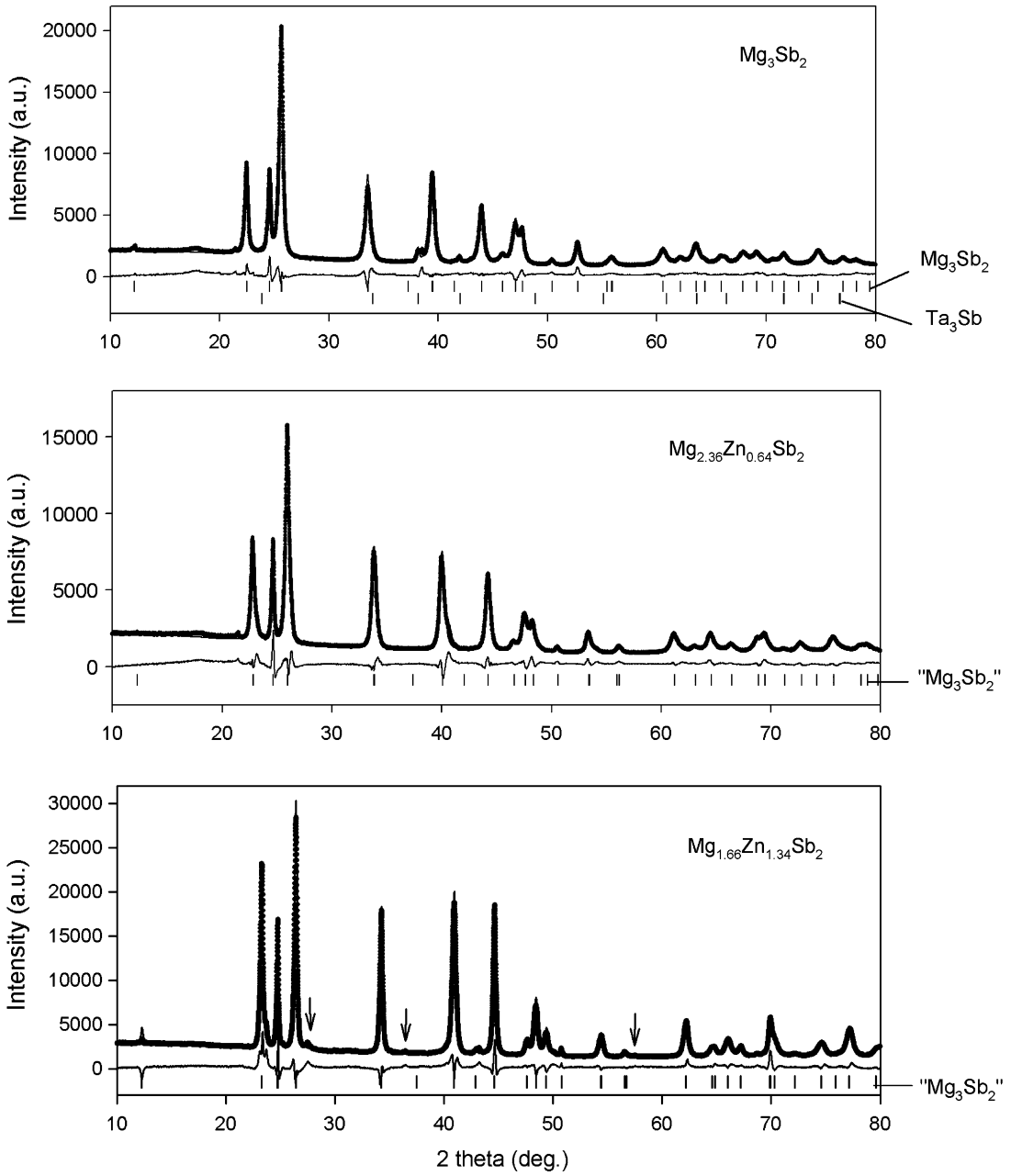

Fig. 1. Rietveld refinement of the powder samples with the initial compositions of Mg_3Sb_2 (top), $Mg_{2.2}Zn_{0.8}Sb_2$ (middle), and $Mg_{1.4}Zn_{1.6}Sb_2$ (bottom). The refined compositions are indicated. The arrows in the bottom figure indicate an unidentified phase.

Table 1
Initial compositions of the samples, refined compositions of the $Mg_{3-x}Zn_xSb_2$ phases and amounts of identified secondary phases in weight percents

Initial composition	Refined composition	Secondary phase
Mg_3Sb_2	Mg_3Sb_2 (p.)[a]	Ta_3Sb 1.93(3)% (p.)
$Mg_{2.6}Zn_{0.4}Sb_2$	$Mg_{2.88(2)}Zn_{0.12(2)}Sb_2$ (p.)	Zn 2.88(5)% (p.)
$Mg_{2.2}Zn_{0.8}Sb_2$	$Mg_{2.36(2)}Zn_{0.64(2)}Sb_2$ (p.)	None
$Mg_{1.8}Zn_{1.2}Sb_2$	$Mg_{1.96(2)}Zn_{1.04(2)}Sb_2$ (p.)	Sb 2.77(3)% (p.)
	$Mg_{1.94(4)}Zn_{1.06(4)}Sb_2$ (s.c.)[a]	
$Mg_{1.4}Zn_{1.6}Sb_2$	$Mg_{1.66(2)}Zn_{1.34(2)}Sb_2$ (p.)	Unidentified

[a]p. and s.c. stand for powder and single crystal methods, respectively.

be easily handled, the hot-pressed pellet of $Mg_{2.2}Zn_{0.8}Sb_2$ was brittle and required extra care during handling. The densities of the hot-pressed Mg_3Sb_2 and $Mg_{2.36}Zn_{0.64}Sb_2$ samples were 3.97(2) and 4.05(2) g/cm^3, which constitute 98% and 90%, correspondingly, of the X-ray densities.

The X-ray powder analysis was performed on both hot-pressed samples to check for impurities or phase changes. No other secondary phase except for the one detected earlier in Mg_3Sb_2 was found and no phase transformation was observed in either of the hot pressed samples. Small pieces from the hot-pressed samples were polished and their composition/surface was analyzed through the

Table 2
Powder refinement data for the Mg_3Sb_2, $Mg_{2.2}Zn_{0.8}Sb_2$, and $Mg_{1.4}Zn_{1.6}Sb_2$ samples at 293 K, Cu$K\alpha_1$ radiation, $2\theta = 10-80^\circ$, step 0.005°, Huber image plate Guinier camera

Initial composition	Mg_3Sb_2	$Mg_{2.2}Zn_{0.8}Sb_2$	$Mg_{1.4}Zn_{1.6}Sb_2$
Refined composition	Mg_3Sb_2	$Mg_{2.36(2)}Zn_{0.64(2)}Sb_2$	$Mg_{1.66(2)}Zn_{1.34(2)}Sb_2$
Sp. gr. (Pearson sym.)	$P\bar{3}m1$ (*hP5*)	$P\bar{3}m1$ (*hP5*)	$P\bar{3}m1$ (*hP5*)
Lattice parameters (Å)	$a = 4.55876(7)$	$a = 4.49450(8)$	$a = 4.40239(5)$
	$c = 7.2274(2)$	$c = 7.2083(2)$	$c = 7.1194(1)$
Volume (Å^3)	130.079(4)	126.131(5)	120.502(3)
Z	1	1	1
Reflections	48	48	45
Atomic param. refined	5	6	6
R_I	0.023	0.017	0.062
R_P	0.046	0.052	0.064
R_{wP}	0.059	0.071	0.089

$R_I = \Sigma|I_o - I_c|/\Sigma|I_o|$, $R_P = \Sigma|y_{oi} - y_{ci}|/\Sigma|y_{oi}|$, $R_{wP} = (\Sigma w_i(y_{oi}\text{-}y_{ci})^2/\Sigma w_i(y_{oi})^2)^{1/2}$, $w_i = (y_{oi})^{-1/2}$.

Table 3
Atomic and isotropic temperature factor (B) parameters for Mg_3Sb_2, $Mg_{2.36(2)}Zn_{0.64(2)}Sb_2$, and $Mg_{1.66(2)}Zn_{1.34(2)}Sb_2$ from the powder diffraction data

Atom		Occup.	x/a	y/b	z/c	B (Å^2)
Mg_3Sb_2						
Mg1	1*a*	1	0	0	0	1.2(2)
Mg2	2*d*	1	1/3	2/3	0.3718(4)	0.40(8)
Sb	2*d*	1	1/3	2/3	0.7682(2)	0.39(2)
$Mg_{2.36(2)}Zn_{0.64(2)}Sb_2$						
Mg1	1*a*	1	0	0	0	0.46(2)
Mg/Zn(2)	2*d*	0.68/0.32(1)	1/3	2/3	0.3719(2)	0.60(7)
Sb	2*d*	1	1/3	2/3	0.7646(2)	0.38(2)
$Mg_{1.66(2)}Zn_{1.34(2)}Sb_2$						
Mg1	1*a*	1	0	0	0	1.4(2)
Mg/Zn(2)	2*d*	0.33/0.67(1)	1/3	2/3	0.3760(3)	0.30(5)
Sb	2*d*	1	1/3	2/3	0.7587(2)	0.19(2)

Table 4
Single crystal data and structure refinements of $Mg_{2.23(1)}Zn_{0.77(1)}Sb_2$ and $Mg_{1.94(4)}Zn_{1.06(4)}Sb_2$ (293 K, Mo$K\alpha$ radiation, Bruker SMART Apex diffractometer)

Composition	$Mg_{2.23(1)}Zn_{0.77(1)}Sb_2$	$Mg_{1.94(4)}Zn_{1.06(4)}Sb_2$
Space group (Pearson symbol)	$P\bar{3}m1$ (*hP5*)	$P\bar{3}m1$ (*hP5*)
Lattice parameters (Å)	$a = 4.4671(5)$	$a = 4.4317(9)$
	$c = 7.195(2)$	*$c = 7.192(3)$*
Data/parameters	139/10	144/10
Goodness-of-fit on F^2	1.114	1.396
Final R indices $[I/\sigma(I) > 2]$	$R_1 = 0.0146$,	$R_1 = 0.0364$,
	$wR_2 = 0.0328$	$wR_2 = 0.0810$
Largest diff. peak/hole (e/Å^3)	0.915/−0.646	2.231/−1.399

energy-dispersive spectroscopy (EDS) technique on the Link Analytical SEM equipped with a Pentafet X-ray microanalyzer. For both samples, the EDS analysis revealed that the surface contained 2–4 at% of oxygen, but the oxygen amount was independent of which part of sample being investigated: both grain boundaries and grains showed statistically identical compositions. It is likely that sample surfaces were slightly oxidized during the sample polishing, as oxidation during the hot pressing would have resulted in the preferential oxidation of the grain boundaries.

The hot-pressed samples were cut into plates and bars of desired size for physical property measurements.

Table 5
Atomic and equivalent isotropic displacement parameters[a] (U_{eq}, Å^2) for $Mg_{2.23(1)}Zn_{0.77(1)}Sb_2$ and $Mg_{1.94(4)}Zn_{1.06(4)}Sb_2$ from the single crystal data

Atom		Occup.	x/a	y/b	z/c	U_{eq}
$Zn_{0.78(1)}Mg_{2.22(1)}Sb_2$						
Mg1	1*a*	1	0	0	0	0.0280(8)
Mg/Zn2	2*d*	0.616/0.384(7)	1/3	2/3	0.3783(2)	0.0241(5)
Sb	2*d*	1	1/3	2/3	0.76865(6)	0.0215(2)
$Mg_{1.94(4)}Zn_{1.06(4)}Sb_2$						
Mg1	1*a*	1	0	0	0	0.034(3)
Mg/Zn2	2*d*	0.47/0.53(2)	1/3	2/3	0.3789(5)	0.024(1)
Sb	2*d*	1	1/3	2/3	0.7664(1)	0.0227(4)

[a]Anisotropic temperature factors and other crystallographic details can be obtained from the authors upon request.

2.5. Physical property measurements

The Seebeck voltage (Fig. 3, solid circles), electrical resistivity (Fig. 4) and thermal conductivity (Fig. 5) of Mg_3Sb_2 and $Mg_{2.36}Zn_{0.64}Sb_2$ ($Mg_{2.36}Zn_{0.64}Sb_2$ is the refined composition from the $Mg_{2.2}Zn_{0.8}Sb_2$ sample) were measured in the 2–290 K region on a QD PPMS instrument. The thermal conductivity was measured using the two-probe configuration of the thermal transport option (TTO) of the QD PPMS. The data were collected in the continuous measurement mode at a cooling rate of 0.2 K/min. Thermal conductivity was automatically evaluated by the TTO software assuming that the infrared emissivity of

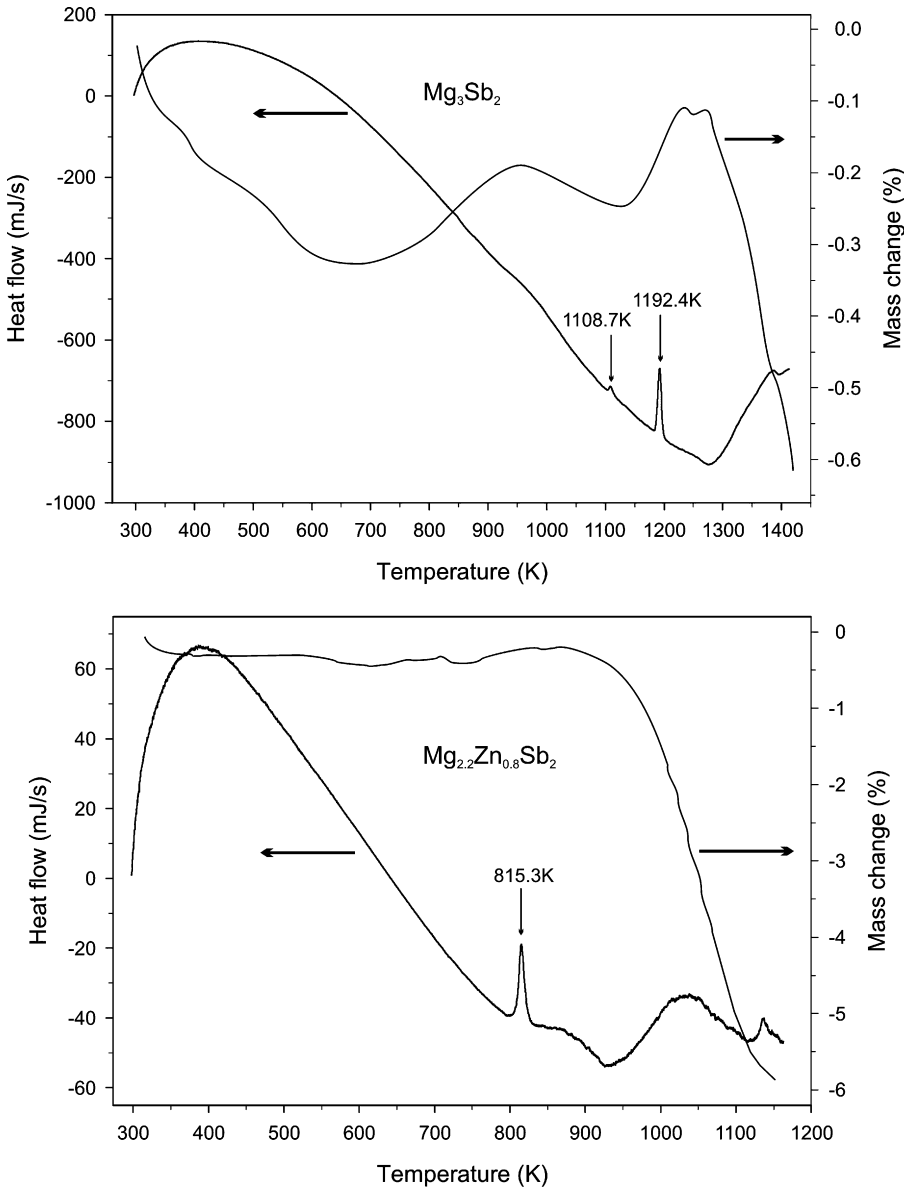

Fig. 2. Variations in mass (TGA) and heat flow (DSC) as a function of temperature for two samples with initial compositions Mg_3Sb_2 and $Mg_{2.2}Zn_{0.8}Sb_2$.

the polycrystalline samples is close to 1. Thermally evaporated Al contacts have been used as contact pads for four-probe electrical resistivity measurements of the samples.

The Seebeck coefficient of 363 μV/K obtained for Mg_3Sb_2 at 290 K was significantly larger than the values reported in literature, e.g. ~250 μV/K at 330 K by Kajikawa et al. [9] or ~25 μV/K at ~310 K by Condron et al. [10]. To verify correctness of our measurements, the Seebeck voltage for Mg_3Sb_2 and $Mg_{2.36}Zn_{0.64}Sb_2$ was re-measured on the home-built apparatus with a He closed-cycle cryostat in the 50–290 temperature range at McMaster University (open circle in Fig. 3). Samples in the shape of a plate were sandwich between the two heaters. Two Cu leads and two thermocouples were attached to the samples with silver epoxy. The heaters allow to reverse the temperature gradient to compensate for any offset in a Seebeck voltage for $\Delta T = 0$. The Seebeck coefficient was calculated as a slope of the Seebeck voltage vs. temperature for each temperature point. As seen from the plots, there is a good correlation between the data obtained on the two instruments.

Since Mg_3Sb_2 exhibits a semiconducting behavior, the temperature range for electrical resistivity measurements was extended to 390 K (Fig. 4) to better evaluate the band gap, as at higher temperatures the conductivity is dominated by the thermal excitation of electrons through the band gap.

2.6. Electronic structure calculations

Tight-binding linear-muffin–tin-orbital calculations using the atomic sphere approximation (TB-LMTO-ASA) [12] were carried out for Mg_3Sb_2 and hypothetical

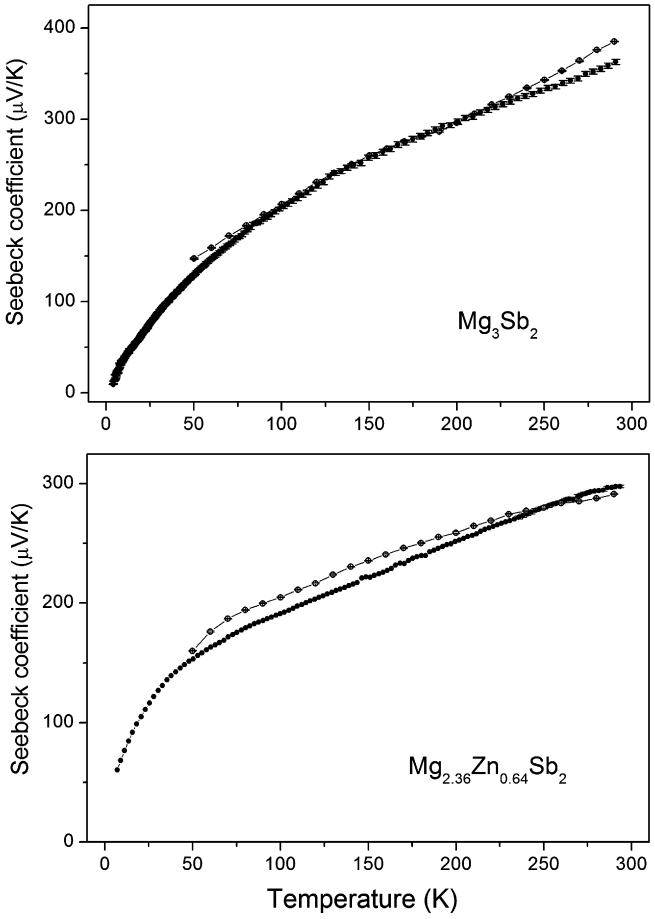

Fig. 3. Seebeck coefficient as a function of temperature for Mg_3Sb_2 and $Mg_{2.36}Zn_{0.64}Sb_2$. Solid symbols are the data obtained on a commercial QD PPMS instrument, open circles are the data obtained on the home-built instrument.

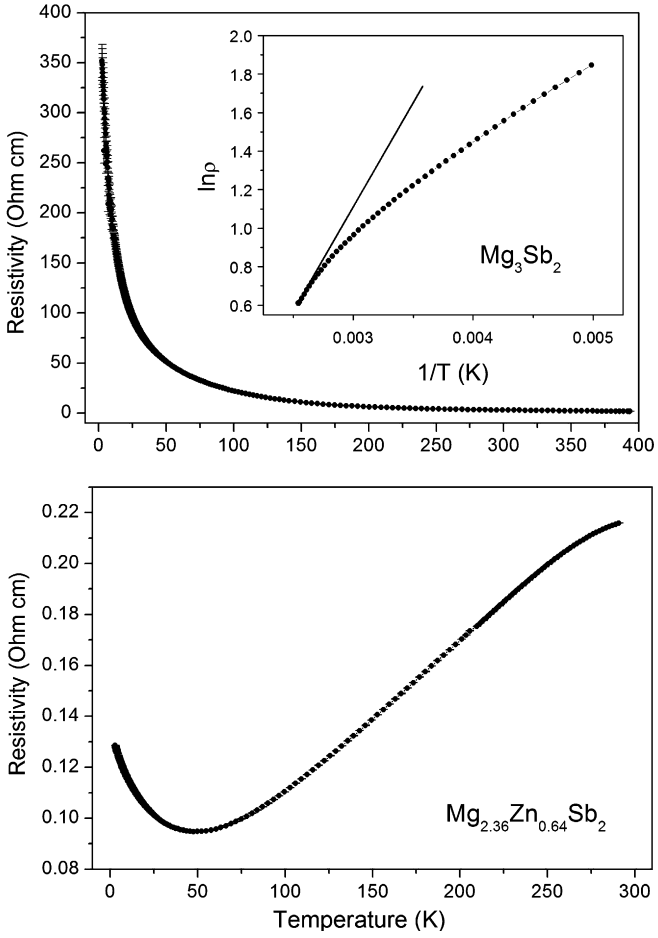

Fig. 4. Resistivity ρ, as a function of temperature for Mg_3Sb_2 and $Mg_{2.46}Zn_{0.64}Sb_2$. Inset in the upper figure shows $\ln\rho$ vs. $1/T$ for Mg_3Sb_2 in the 200–390 K region and the straight line indicates a slope at 390 K.

Mg_2ZnSb_2. For Mg_2ZnSb_2, the structural parameters from the $Mg_{1.94(4)}Zn_{1.06(4)}Sb_2$ single crystal were used and the symmetry was reduced to $P3m1$ to split the $2d$ Mg/Zn2 site into two individual sites. One of this site, namely $1c$, was assumed to be the Zn site. To satisfy the overlap criteria of the atomic spheres in the TB-LMTO-ASA method, empty spheres were included into the unit cell. A tetrahedron integration method was used with a total of 1152 points in the irreducible wedge of the Brillouin zone.

The DOS for Mg_3Sb_2 exhibits a band gap of 0.21 eV and Mg_3Sb_2 is expected to be a semiconductor (Fig. 6). In Mg_2ZnSb_2, the band gap is closed and the phase should be metallic. The DOS calculated for Mg_3Sb_2 using the TB-LMTO-ASA method is very similar to the DOS obtained by Imai et al. using first-principle pseudo-potential method based on the density-functional theory [13]. According to Imai et al. Mg_3Sb_2 should be an indirect-band semiconductor with an energy gap of 0.41 eV.

3. Discussion

The structure of the $Mg_{3-x}Zn_xSb_2$ phases with $x = 0$–1.34 (Fig. 7) is identical to that of anti-La_2O_3 (sp. group $P\bar{3}m1$) assigned for Mg_3Sb_2 [7]. In the anti-La_2O_3 type structure, the metal atoms enter inside the tetrahedra and octahedra formed by the p-elements. The $Mg_{3-x}Zn_xSb_2$ structure keeps the same relative atomic arrangement, with the Zn atoms occupying some of the tetraheda (up to 67%). The tendency of Zn to occupy the tetrahedral voids instead of octahedral ones is well known (e.g. two polymorphs of ZnS:zinc blende and wurtzite) [14] and is due to the fact that the bond-forming orbitals are predominantly the sp^3 ones and not the localized d-ones. From this structural prospective, the $Mg_{3-x}Zn_xSb_2$ structure differs significantly from the structures of other substituted Mg_3Sb_2-based phases, such as $AeMg_2Sb_2$ (Ae is Ca, Sr, or Ba) [15] and $Mg_{5.23}Sm_{0.77}Sb_4$ [16], even neglecting changes in symmetry. In $AeMg_2Sb_2$ and $Mg_{5.23}Sm_{0.77}Sb_4$, the divalent metal substitutes Mg on the octahedral site, while in $Mg_{3-x}Zn_xSb_2$, Zn atoms enter exclusively into the tetrahedral sites.

The preference of Zn atoms for the tetrahedral sites can be also related to the environment around the Mg/Zn2 sites. Much shorter distances to the four neighboring Sb atoms and presence of the six Mg/Zn2 atoms at ~3.1 Å favor the occupancy by smaller atoms and with smaller

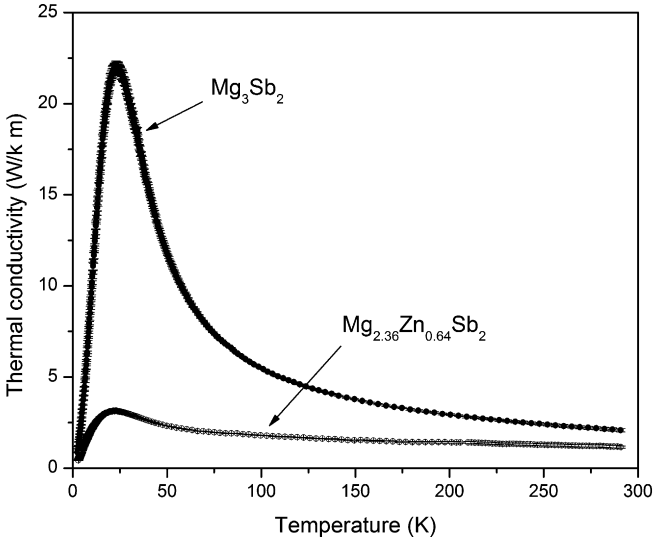

Fig. 5. Thermal conductivity as a function of temperature for Mg_3Sb_2 and $Mg_{2.36}Zn_{0.64}Sb_2$.

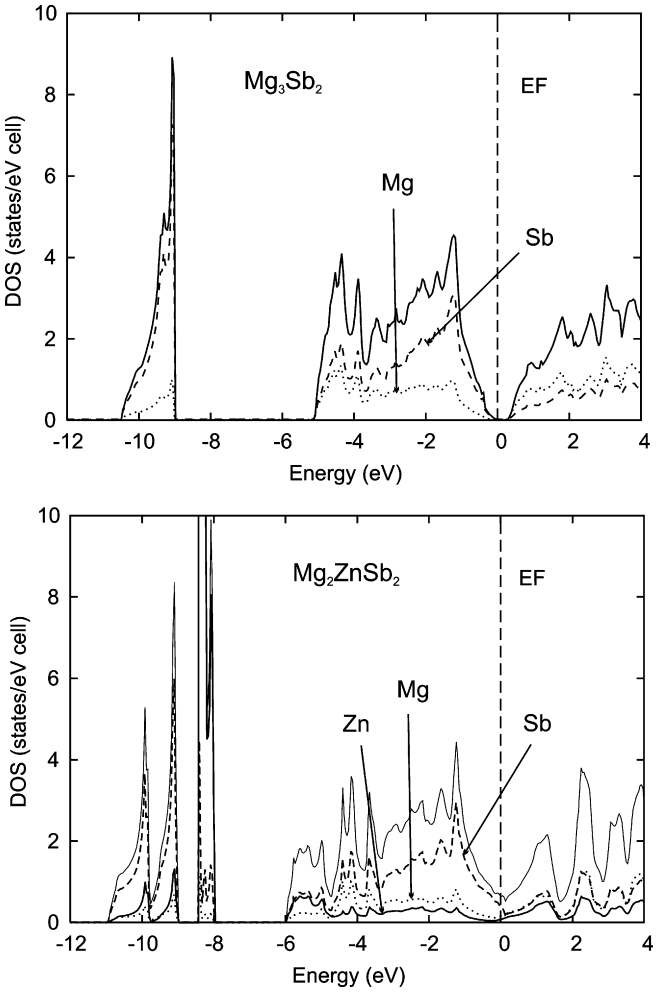

Fig. 6. Densities of states (DOS) for Mg_3Sb_2 and Mg_2ZnSb_2.

positive charges to reduce the Coulomb repulsion. The Zn atoms meet both of these requirements as they have a smaller atomic radius (1.35 vs. 1.50 Å for Mg) [17] as well as a lower electronegativity (1.59 vs. 1.29) [18,19], with the latter factor leading to the lower electrostatic repulsion due to a smaller positive charge on the Zn atoms. Although indirectly, the band structure calculations also suggest smaller positive charge on the Zn atoms, as more states are situated below the Fermi level in case of Mg_2ZnSb_2 as compared with Mg_3Sb_2 and these states have a substantial contribution from the Zn orbitals (Fig. 6).

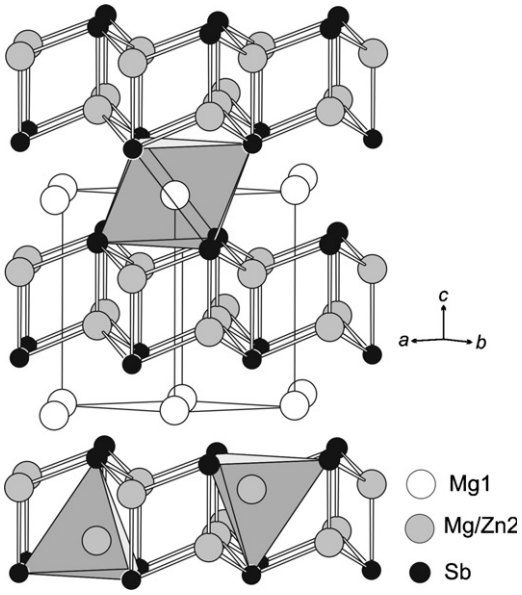

Fig. 7. Structure of the $Mg_{3-x}Zn_xSb_2$ phases. Antimony octahedra and tetrahedra around Mg1 and Mg/Zn2 and Mg/Zn3 are shown.

A full substitution of the 2*d* site by the Zn atoms would yield a phase with the $MgZn_2Sb_2$ composition, whose synthesis was attempted but failed. The maximum Zn concentration on the 2*d* site, observed in our experiments, is likely to limit the homogeneity range for the $Mg_{3-x}Zn_xSb_2$ phases to $x = 1.34$. It may be still possible to achieve Zn-richer phases, but this may require adjustment of the preparation procedures.

The DSC curve for Mg_3Sb_2 (Fig. 2) points at two endothermic solid–solid transitions at elevated temperatures: one at 1109 K and the other at 1192 K. The latter transition point is close to and can be associated with the polymorphic transformation temperature of 1203 ± 2 K reported for α-$Mg_3Sb_2 \leftrightarrow \beta$-$Mg_3Sb_2$ [20]. We believe that the room-temperature structure of Mg_3Sb_2 we have established corresponds to the α-polymorph. Above 1273 K, the Mg_3Sb_2 phase starts to loose mass as is apparent from the sharp mass drop and the endothermic character of the heat flow curve. Contrary to the observation by Condron et al. [10], we do not see any significant oxidation or mass losses up to 1273 K, which can be attributed to the reducing atmosphere during our experiment that prevented the sample oxidation and the faster heating rate.

Room-temperature physical properties for Mg_3Sb_2 and $Mg_{2.36}Zn_{0.64}Sb_2$ (from the $Mg_{2.2}Zn_{0.8}Sb_2$ sample) are summarized in Table 6. Presence of small quantities

Table 6
Some physical parameters of Mg_3Sb_2 and $Mg_{2.36}Zn_{0.64}Sb_2$ at room temperature

Property	Mg_3Sb_2	$Mg_{2.36}Zn_{0.64}Sb_2$
X-ray density (g/cm^3)	4.038	4.453
Resistivity (Ω cm)	3.30	0.216
Band gap (eV)	0.18	0
Seebeck coefficient (μV/K)	363	298
Thermal conductivity (W/K m)	2.08	1.16
Figure-of-merit, ZT	5.56×10^{-4}	1.03×10^{-2}

(~2 wt%) of metallic Ta_3Sb is unlikely to influence the Seebeck coefficient and thermal conductivity to a significant extend. We found no published data on the physical properties of Ta_3Sb except that it becomes superconducting at 0.59–0.72 K [21] suggesting that Ta_3Sb is metallic at higher temperatures. Assuming the resistivity of Ta_3Sb to be similar to that of Ta, the resistivity of Mg_3Sb_2 is underestimated only by ~5% across the studied temperature range according to the resistvity-mixture rule for a highly conductive disperse phase [22]. Therefore the value given in Table 6 are expected to be close to those for pure Mg_3Sb_2.

We will compare only the Mg_3Sb_2 results with the literature data, as no data for the Zn-doped phase have been reported. Since the literature data are for temperatures above 300 K, we will contrast our room-temperature data with the literature ones for the lowest temperature reported. The room-temperature Seebeck coefficient of 363 μV/K for Mg_3Sb_2 is larger than value of ~250 μV/K reported by Kajikawa et al. [9] for 330 K and is much larger than ~25 μV/K reported by Condron et al. [10] for ~310 K. The Mg_3Sb_2 resistivity of 3.30 Ω cm is higher than ~0.08 Ω cm by Kajikawa et al. but lower than ~50 Ω cm by Condron et al. The value of the thermal conductivity of 2.08 W/K m is close to ~2 W/K m given by Kajikawa et al. but lower than ~4.2 W/K m reported by Condron et al. Although some of our results are closer to those from Kajikawa et al. there is still a significant difference. As pointed out by Condron et al. [10], different preparation techniques are likely to be the cause for different values observed.

The curve of $\ln \rho$ vs. $1/T$ for Mg_3Sb_2 (inset in Fig. 4 for the 200−390 K range) does not show a linear behavior expected for intrinsic semiconductors but rather indicates that different mechanisms contribute to the electrical conductivity. Assuming that at 390 K the electrical conductivity is dominated by the thermal excitation of electrons through the band gap, the band gap is estimated to be ~0.18 eV. This value is close to 0.21 eV obtained from our LMTO calculations but is significantly smaller than the value of 0.82 eV reported by Busch et al. [23]. Temperature dependence of the Seebeck coefficient in the 2–290 K range also does not support the model of a purely intrinsic, narrow-band semiconductor, since in the latter case the thermopower should show divergence at low temperatures [24]. The monotonous decrease of the Seebeck coefficient with decreasing temperature rather suggests an Anderson-type localization of the charge carriers at a finite density of states uniformly distributed within the band gap. The extrinsic origin of these in-gap states could be attributed to impurities or a lattice disorder which may account for a large discrepancy in the both Seebeck and the conductivity data reported in literature.

The substitution of Zn for Mg renders $Mg_{2.36}Zn_{0.64}Sb_2$ metallic (Fig. 4) which is indicative of disappearance of the band gap. This conclusion is supported by the electronic structure calculations for a Zn-richer composition, Mg_2ZnSb_2 (Fig. 6). The resistivity of $Mg_{2.36}Zn_{0.64}Sb_2$ (ρ = 0.216 Ω cm) is lower than that of Mg_3Sb_2 (ρ = 3.30 Ω cm), however it is still too large to make $Mg_{2.36}Zn_{0.64}Sb_2$ a competitive thermoelectric material; e.g. the resistivity of "Zn_4Sb_3" is 0.0015 Ω cm at 290 K [5]. Thermal conductivity, 1.16 W/K m, of $Mg_{2.36}Zn_{0.64}Sb_2$ at room temperature is lower than that of Mg_3Sb_2 and is a consequence of more effective phonon scattering on the mixed Mg/Zn sites. Also, relatively small temperature dependence of the thermal conductivity supports the fact that the phonon propagation in the structure is limited by the Zn/Mg disorder. The thermal conductivity of both $Mg_{2.36}Zn_{0.64}Sb_2$ and Mg_3Sb_2 is comparable to those of the high-performance thermoelectric materials such as $(Sb,Bi)_2Te_3$, and PbTe, Te/Ag/Ge/Sb alloys [25].

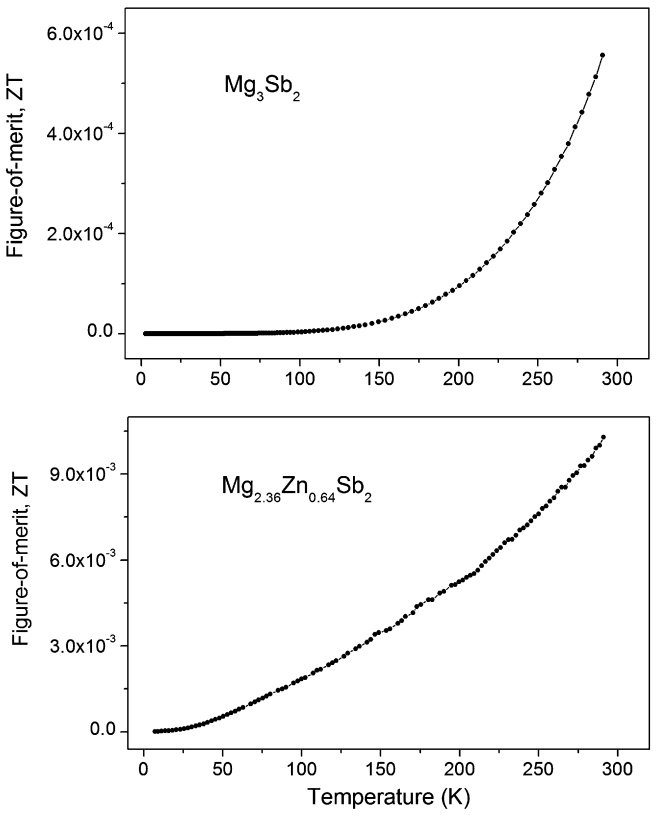

Fig. 8. Dimensionless figure-of-merit as a function of temperature for Mg_3Sb_2 and $Mg_{2.36}Zn_{0.64}Sb_2$.

The dimensionless figure-of-merit, ZT, as a function of temperature for Mg_3Sb_2 and $Mg_{2.36}Zn_{0.64}Sb_2$ is shown in Fig. 8. The ZT is 18-times larger for $Mg_{2.36}Zn_{0.64}Sb_2$, which is mostly due to its lower electrical resistivity. Still, $Mg_{2.36}Zn_{0.64}Sb_2$ falls short in performance compared to "Zn_4Sb_3" [1] or other materials, and this is mostly because of its electrical resistivity which while being lower compared to Mg_3Sb_2 is much larger compared to other thermoelectric materials.

Acknowledgment

This work was supported by a Discovery Grant from the Natural Sciences and Engineering Research Council of Canada.

Appendix A. Supporting information

Supplementary data associated with this article can be found in the online version at doi:10.1016/j.jssc.2007.06.011.

References

[1] T. Caillat, J.P. Fleurial, A. Borshchevsky, J. Phys. Chem. Solids 58 (7) (1997) 1119–1125.
[2] G.J. Snyder, M. Christensen, E. Nishibori, T. Caillat, B.B. Iversen, Nat. Mater. 3 (7) (2004) 458–463.
[3] F. Cargnoni, E. Nishibori, P. Rabiller, L. Bertini, G.J. Snyder, M. Christensen, C. Gatti, B.B. Iversen, Chem.-Eur. J. 10 (16) (2004) 3861–3870.
[4] J. Nylen, M. Andersson, S. Lidin, U. Haeussermann, J. Am. Chem. Soc. 126 (50) (2004) 16306–16307.
[5] Y. Mozharivskyj, Y. Janssen, J.L. Harringa, A. Kracher, A.O. Tsokol, G.J. Miller, Chem. Mater. 18 (3) (2006) 822–831.
[6] Y. Mozharivskyj, A.O. Pecharsky, S. Bud'ko, G.J. Miller, Chem. Mater. 16 (8) (2004) 1580–1589.
[7] E. Zintl, E. Husemann, Z. Phys. Chem. B 21 (1933) 138–155.
[8] A.S. Mikhaylushkin, J. Nylen, U. Haeussermann, Chem.-Eur. J. 11 (17) (2005) 4912–4920.
[9] T. Kajikawa, N. Kimura, T. Yokoyama, Proceedings of the 22nd International Conference on Thermoelectrics, 2003, pp. 305–308.
[10] C.L. Condron, S.M. Kauzlarich, F. Gascoin, G.J. Snyder, J. Solid State Chem. 179 (8) (2006) 2252–2257.
[11] XRD Single Crystal Software, Bruker AXS Inc., Madison, USA, 2002.
[12] O.K. Andersen, Z. Pawlowska, O. Jepsen, Phys. Rev. B 34 (8 Part 1) (1986) 5253–5269.
[13] Y. Imai, A. Watanabe, J. Mater. Sci. 41 (8) (2006) 2435–2441.
[14] A.R. West, Basic Solid State Chemistry, Wiley, New York, 1996, p. 334.
[15] K. Deller, B. Eisenmann, Z. Naturforsch. 32B (6) (1977) 612–616.
[16] S. Gupta, A.K. Ganguli, J.D. Corbett, Inorg. Chem. 45 (20) (2006) 8175–8178.
[17] J.C. Slater, J. Chem. Phys. 41 (10) (1964) 3199–3204.
[18] J.B. Mann, T.L. Meek, L.C. Allen, J. Am. Chem. Soc. 122 (12) (2000) 2780–2783.
[19] J.B. Mann, T.L. Meek, E.T. Knight, J.F. Capitani, L.C. Allen, J. Am. Chem. Soc. 122 (21) (2000) 5132–5137.
[20] T.B. Massalski, H. Okamoto, P.R. Subramanian, L. Kacprzak, Binary Alloy Phase Diagrams, ASM International, USA, 1990.
[21] H.L. Luo, E. Vielhaber, E. Corenzwit, Z. Phys. 230 (5) (1970) 443–448.
[22] S.O. Kasap, Principles of Electronic Materials and Devices, third ed, McGraw-Hill, Boston, 2006.
[23] G. Busch, F. Hulliger, U. Winkler, Helv. Phys. Acta 27 (1954) 195–196, 249–258.
[24] P.M. Chaikin, Proceedings of the International Conference on Organic Superconductors, 1990, pp. 101–115.
[25] D.M. Rowe, Thermoelectrics Handbook, CRC Press, Boca Raton, FL, 2006.